scientific reports

Check for updates

OPEN

Bioinspired palladium-doped manganese oxide nanocorns: a remarkable antimicrobial agent targeting phyto/animal pathogens

Sagar Vikal[1], Yogendra K. Gautam[1]✉, Ashwani Kumar[2,5]✉, Ajay Kumar[3]✉, Jyoti Singh[4], Dharmendra Pratap[4], Beer Pal Singh[1] & Neetu Singh[3]

Microbial pathogens are known for causing great environmental stress, owing to which emerging challenges like lack of eco-friendly remediation measures, development of drug-resistant and mutational microbial strains, etc., warrants novel and green routes as a stepping stone to serve such concerns sustainably. In the present study, palladium (Pd) doped manganese (II, III) oxide (Mn_3O_4) nanoparticles (NPs) were synthesized using an aqueous *Syzygium aromaticum* bud (ASAB) extract. Preliminary phytochemical analysis of ASAB extract indicates the presence of polyphenolics such as phenols, alkaloids, and flavonoids that can act as potential capping agents in NPs synthesis, which was later confirmed in FTIR analysis of pure and Pd-doped Mn_3O_4 NPs. XRD, Raman, and XPS analyses confirmed the Pd doping in Mn_3O_4 NPs. FESEM and HRTEM study reveals the mixed morphologies dominated by nanocorns appearance. Zeta potential investigation reveals high stability of the synthesized NPs in colloidal solutions. The developed Pd-doped Mn_3O_4 NPs were tested against two fungal phytopathogens, i.e., *Sclerotinia sclerotiorum* and *Colletotrichum gloeosporioides*, known for causing great economic losses in yield and quality of different plant species. The antifungal activity of synthesized Pd-doped Mn_3O_4 NPs displayed a dose-dependent response with a maximum of ~92%, and ~72% inhibition was recorded against *S. sclerotiorum* and *C. gloeosporioides*, respectively, at 1000 ppm concentration. However, *C. gloeosporioides* demonstrated higher sensitivity to Pd-doped Mn_3O_4 NPs upto 500 ppm) treatment than *S. sclerotiorum*. The prepared NPs also showed significant antibacterial activity against *Enterococcus faecalis*. The Pd-doped Mn_3O_4 NPs were effective even at low treatment doses, i.e., 50–100 ppm, with the highest Zone of inhibition obtained at 1000 ppm concentration. Our findings provide a novel, eco-benign, and cost-effective approach for formulating a nanomaterial composition offering multifaceted utilities as an effective antimicrobial agent.

Abbreviations

ADDA	Agar disc diffusion assay
ASAB	Aqueous *Syzygium aromaticum* bud
CB	Conduction band
DDW	Double-distilled water
DNA	Deoxy ribose nucleic acid
EDAX	Energy dispersive X-ray analysis
ETC	Electron transport chain
eV	Electron volt
FESEM	Field emission scanning electron microscopy
FTIR	Fourier-transform infrared spectroscopy

[1]Smart Materials and Sensors Laboratory, Department of Physics, Chaudhary Charan Singh University, Meerut, Uttar Pradesh 250004, India. [2]Nanoscience Laboratory, Institute Instrumentation Centre, IIT Roorkee, Roorkee 247667, India. [3]Department of Biotechnology, Mewar Institute of Management, Ghaziabad, Uttar Pradesh 201012, India. [4]Plant Molecular Virology Laboratory, Department of Genetics and Plant Breeding, Chaudhary Charan Singh University, Meerut, Uttar Pradesh 250004, India. [5]Department of Physics, Graphic Era (Deemed to Be University), Dehradun, Uttarakhand 248002, India. ✉email: ykg.iitr@gmail.com; 01ashraj@gmail.com; ajaykmr1986@gmail.com

HCl	Hydrochloric acid
JCPDS	Joint Committee on Powder Diffraction Standards
KOH	Potassium hydroxide
mm	Milli meter
mM	Milli molar
Mn	Manganese
Mn_3O_4	Manganese (II, III) oxide
$MnCl_2{\cdot}4H_2O$	Manganese chloride tetrahydrate
MNPs	Metallic nanoparticles
NaCl	Sodium chloride
NaOH	Sodium hydroxide
NBM	Nutrient broth media
nm	Nanometer
Pd	Palladium
PDA	Potato dextrose agar
$PdCl_2$	Palladium chloride
ppm	Parts per million
ROS	Reactive oxygen species
SAED	Selected area electron diffraction
SPM	Solid media plates
TEM	Transmission electron microscopy
VB	Valence band
w/v	Weight by volume
XPS	X-ray Photoelectron Spectroscopy
XRD	X-Ray diffraction
ZOI	Zone of Inhibition
ZP	Zeta potential

Nanobiotechnology integrates biotechnology and nanotechnology, dealing with applications of nanomaterials in biological sciences[1–4]. With the advent of nanobiotechnology, nanostructures' biological and physiochemical properties are tuned to serve the most relevant areas of human welfare, like medicine and agriculture[5]. Among different types, metallic nanoparticles (MNPs) are one of the widely exploited antimicrobial nanomaterials against phyto- and animal pathogens[6–12]. Researchers have recently witnessed a growing interest in synthesizing biocompatible metal-based NPs, utilizing green chemistry and bioinspired fabrication routes[13–21].

Biological synthesis offers an eco-friendly and cost-effective method for the fabrication of NPs[22] and is preferred over conventional methods[23]. Different biogenic sources for the synthesis of MNPs, like bacteria, plants, algae, fungi, yeasts, and actinomycetes, cause considerable modifications in the properties of their corresponding metals[24]. Among such sources, plant-based bioinspired fabrication of NPs is one of the preferred approaches[24,25]. The bioactive compounds in plant extracts can act as potential reducing and capping agents in synthesizing MNPs[24,25]. Green synthesis of MNPs like silver, copper, gold, iron, titanium, zinc, platinum, palladium, etc., has been extensively investigated[26–28]. However, limited investigations for green synthesis of manganese (Mn) NPs have been reported so far[24], despite various applications in catalysis, biomedicine, electronics, electrochemistry, energy, optics, biosensors, food, pharmaceutical, cosmetics, textile industries, etc.[24,29].

Metal oxides such as ZnO, CuO, TiO_2 and MnO etc. have also a great potential to have excellent antimicrobial activity[19]. Chamaecostus cuspidatus extract is used to green synthesis CeO_2 and ZnO nanoparticles (NPs) and effective antibacterial activities. The anticancer effects of CeO_2 and ZnO nanoparticles were investigated in human breast cancer cell lines[21]. Similarly, Green synthesis is used to prepare Cerium oxide nanoparticles (CeO_2 NPs) from Artabotrys hexapetalus leaf extracts. The prepared NPs exhibit excellent antibacterial activity against a variety of bacterial species. The anticancer potential of the compound was studied against the (MCF-7) human breast cancer cell line[22]. In addition to that, Zinc oxide nanoparticle (ZnO NPs) was prepared utilizing starch in a single step green synthesis and had highly porous, novel hollow multi-sphere in morphology. Because of their morphology and porosity, the synthesized ZnO NPs can be employed in a variety of drug delivery applications[19]. Mn has been reported as the transition element with the third highest abundance on earth followed by iron and titanium[30]. Among various 3d transition metal-oxides, Mn-oxides (MnO, MnO_2, Mn_2O_3, Mn_3O_4, and Mn_5O_8) have obtained key attention owing to their compositional and structural diversity[24,31]. Mn-oxides NPs also possess structural adaptability with varying physicochemical qualities[32]. Mn-oxide NPs have excessive potential for sustainable-nanotechnology research and innovation[24,30]. Mn-oxides can have applications in optoelectronics, magnetic storage devices, imaging contrast agents, magnetic materials, drug delivery, catalysis, wastewater treatment, solar cells, etc.[24].

Sclerotinia sclerotiorum is a necrotrophic phytopathogen that harbors a broad host range and causes stem rot disease in different crops including soybean, oilseed rape, sunflower, tomato, etc., resulting huge losses of agricultural produce[33]. On the other hand, *C. gloeosporioides* follows the hemibiotrophic infection mode and is known for causing anthracnose in fruits like papaya, mango, avocado, apple, guava, banana, papaya, cashews, grapes, pitaya, etc., resulting in serious postharvest losses[34,35]. Although chemical fungicides have been utilized for their control, their indiscriminate utilization has serious environmental consequences that necessitate the search for novel and eco-friendly alternatives[36]. *E. faecalis* is known to colonize the human intestine, and its occurrence in aquatic bodies implies fecal contamination[37]. These bacteria have been reported as multidrug-resistance microbial pathogens associated with hospital-acquired infections[37,38].

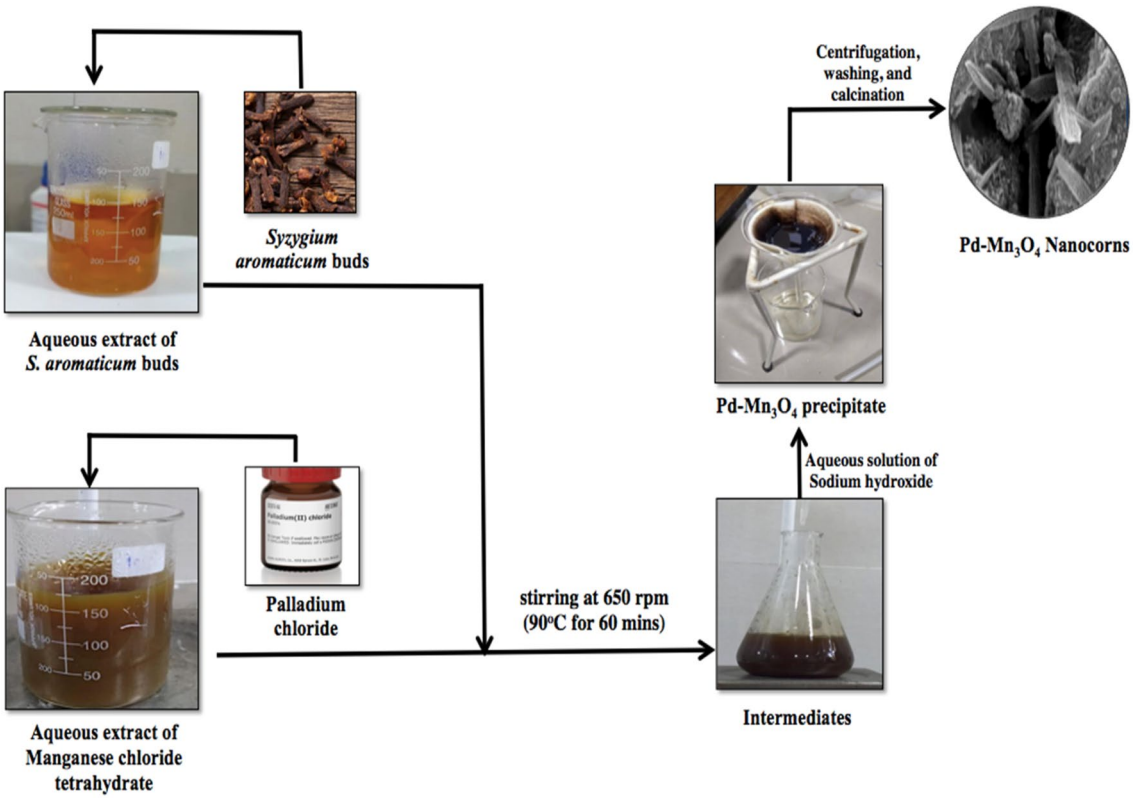

Figure 1. Schematic of the green synthesis of pure and Pd-doped Mn_3O_4 NPs.

To combat such underlying issues, present study focused on developing nanoformulation comprised of Pd-doped Mn_3O_4 NPs through the green chemistry route as a potential tool to offer a broad spectrum of antimicrobial activity.

In the current study, green synthesis of Mn_3O_4 NPs was completed by using *Syzygium aromaticum* bud extract as a potential reducing and capping agent. Adding novelty to this work, attempts were made to modify the structural attributes of Mn_3O_4 NPs through Pd doping to prioritize their multifaced applications in sectors such as agriculture, environment and medicine. To the best of our knowledge and available literature, this is the first report on the bioinspired fabrication of nanocorn-like Pd-doped Mn_3O_4 NPs using ASAB extract.

This present work investigated the antimicrobial potential of bioinspired Pd-doped Mn_3O_4 NPs against *S. sclerotiorum*, *C. gloeosporioides*, and *E. faecalis*.

Experimental

Materials and methods. All the chemicals used in the present study (such as manganese chloride tetrahydrate, palladium chloride, sodium hydroxide, dextrose, agar, hydrochloric acid, potassium hydroxide, sodium chloride, yeast extract, beef extract, and peptone) were of analytical grade and utilized without any further purifications. The solutions and reagents were prepared in double-distilled water (DDW).

Collection of plant material. The evenly looking dried flower buds of *S. aromaticum* were obtained from the nearby local market of Meerut (Uttar Pradesh, India). The taxonomical evaluation was performed by Prof. Vijai Malik, Head, Department of Botany, CCS University, Meerut (UP) (letter reference no. Bot/PB/380). Plant material was procured as per applicable Institutional, International, and National guidelines. The specimens were deposited in the University Herbarium at the Department of Botany (Accession no. Bot. 26 V_2L_4).

Preparation of *S. aromaticum* bud extract. The procured flower buds were thoroughly washed with distilled water to remove dirt particles and dried at 40 °C for 48 h. The dried flower buds were homogenized into a fine powdered form and stored in an air-tight container until used. To prepare the extract, powdered flower buds were macerated in DDW (1:10, w/v) at 60 °C for 2 h. After cooling at room temperature, the aqueous solution of phytoextract was filtered using Whatman filter paper number 1 at stored at 4 °C temperature until use.

Green synthesis of pure and Pd-doped Mn_3O_4 nanoparticles. The NPs were synthesized using a sol–gel method[39], assisted by the addition of phytoextract as a potential source of capping agent (Fig. 1). Briefly, 2% (w/v) $PdCl_2$ was added to the aqueous solution of $MnCl_2.4H_2O$ (49 mM) followed by drop-wise addition of 10 ml aqueous *Syzygium aromaticum* bud extract under continuous stirring at 650 rpm at 90 °C for one hour. After getting the light brown color of the solution, 25 mM aqueous solution of NaOH was added drop-wise to

adjust the pH. The alkali-mediated synthesis provides rapid precipitation leading to the mixture of manganese dihydroxide (Mn $(OH)_2$) and manganese trihydroxide (Mn $(OH)_3$)[40,41]. The appearance of a dark brownish-black precipitate indicated the formation of Pd-doped Mn_3O_4 NPs. The precipitate was collected using centrifugation at 5000 rpm for 10 min. The recovered precipitate gave multiple washings with ethanol and DDW to remove impurities, then dried at 150 °C for 3.5 h in a hot air oven. The finally dried residue was transformed into fine powder through mechanical grinding. The obtained Mn_3O_4 NPs were stored in an airtight bottle for further characterization. Except for the dopant addition, all other synthesis steps for pure Mn_3O_4 NPs were the same as those mentioned for Pd-doped Mn_3O_4 NPs. The key reaction steps in synthesizing Mn_3O_4 NPs are mentioned below[40].

$$MnCl_2 \cdot 4H_2O \rightleftharpoons Mn^{2+} + 2Cl^- + 4H_2O \quad (1)$$

$$2\,Mn^{+} \overset{NaOH}{\rightleftharpoons} Mn\,(OH)_2 + Mn\,(OH)_3 \quad (2)$$

$$Mn\,(OH)_2 + Mn(OH)_3 \overset{Calcination}{\longrightarrow} Mn_3O_4 + 4H_2O \quad (3)$$

Characterization of synthesized nanoparticles. XRD analysis was performed to study the crystallinity and phases of prepared NPs (Bruker AXS, D8 Advance). The phase transitions and chemical composition of synthesized NPs were examined by Raman spectroscopy. The morphology and elemental composition were studied by FESEM (FEI, Quanta 200F), and EDAX, respectively. FTIR analysis conducted on ASAB extract and synthesized NPs to investigate the role of bioactive compounds in the development of NPs. The zeta potential and structural properties were determined using Zetasizer (Malvern Nano ZS) and HRTEM/SAED, respectively. XPS analysis was conducted to study the composition, and oxidation states of Pd-doped Mn_3O_4 NPs. The optical properties of prepared NPs were determined by UV–Visible spectroscopy.

Antimicrobial activity of nanoparticles. The antifungal activity of NPs was tested against *S. sclerotiorum* and *C. gloeosporioides* using the poisoned food technique. The fungal cultures were procured from Indian Type Culture Collection (ITCC), Division of Plant Pathology, Indian Agriculture Research Institute, New Delhi, India. The potato dextrose agar (PDA) media was prepared for fungal growth with following composition: dextrose (2% w/v), potato starch (0.4% w/v), and agar (1.5% w/v). The pH of 5.6 ± 0.2 was adjusted using 0.1N KOH/0.1N HCl. The synthesized NPs were dispersed in PDA media to get the desired concentrations (up to 1000 ppm). The media containing NPs was poured into a Petri plate. At the next step, a ~ 8 mm piece of actively growing mycelia from 5 to 8 days old pure cultures of *S. sclerotiorum* and *C. gloeosporioides* were placed in the middle of each plate and incubated for five days at ~ 25 ± 2 °C and ~ 28 ± 2 °C temperature, respectively. The media plates without NPs treatment served as the negative control, and plates with 2 mg/ml of carbendazim + mancozeb were designated as the positive control. The % of growth inhibition was calculated using the below formula:

$$\frac{(\text{Growth in Control plates} - \text{Growth in treatment plates})}{\text{Growth in Control plates}} \times 100 \quad (4)$$

The antibacterial activity of NPs was determined using agar disc diffusion assay (ADDA). The pure culture of *E. faecalis* was inoculated to freshly prepared nutrient broth media (NBM) and maintained at 37 °C for ~ 18 h. The composition of NBM was Yeast extract (0.2% w/v), Beef extract (0.1% w/v), Peptone (0.5% w/v), NaCl (0.5% w/v), and pH ~ 7.4 ± 0.2. 2% (w/v) agar was added to the nutrient broth for preparing solid media plates (SPM). The pure culture of *E. faecalis* at the active log phase was uniformly spread on SPM. The sterile filter paper discs of about 6 mm diameter, each dipped in various concentrations of NPs (0 to 1000 ppm), were placed on SPM. The DDW-dipped discs were served as a negative control. The Petri plates were placed in an incubator overnight, and the ZOI was measured in millimetre. All the experiments on antimicrobial activity were performed in triplicates under aseptic conditions in a laminar airflow chamber. The nutrient media, glassware, and other utilities were autoclaved at 121 °C for 15 min at 15 psi pressure before use to maintain aseptic conditions throughout the assay.

Statistical analysis. All of the experiments were completed in triplicates and recorded data presented as mean ± standard deviation using Microsoft Excel®.

Results and discussion

Green synthesis of nanoparticles and FTIR analysis. Pure and Pd-doped Mn_3O_4 NPs were synthesized using an aqueous *Syzygium aromaticum* bud (ASAB) extract. Preliminary phytochemical analysis indicated the presence of phenols (ferric chloride test)[42], flavonoids (lead acetate test)[43], alkaloids (Wagner test), carbohydrates (fehling's test), and tannins (ferric chloride test)[44]. The results were in concordance with the findings of Jimoh et al.[43], which established the suitability of the tested plant as a potential substrate for developing Phyto inspired nanoparticles[45–47]. Through FTIR analysis, Rajesh et al.[45] predicted the role of metabolites present in *S. aromaticum* bud extract, such as flavonoids, tannins, alkaloids, and carotenoids, in the green synthesis of CuNPs. We have compared the FTIR spectra of ASAB extract, pure and Pd-doped Mn_3O_4 NPs to validate the capping and stabilizing potential of bioactive compounds present in phytoextract (Fig. 2).

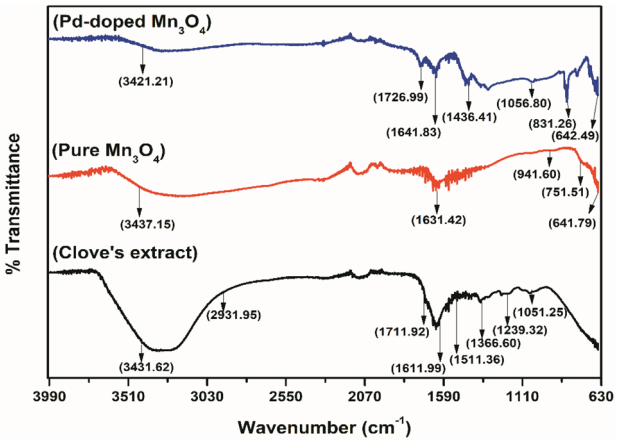

Figure 2. FTIR spectra of ASAB (clove) extract, pure, and Pd-doped Mn_3O_4 NPs.

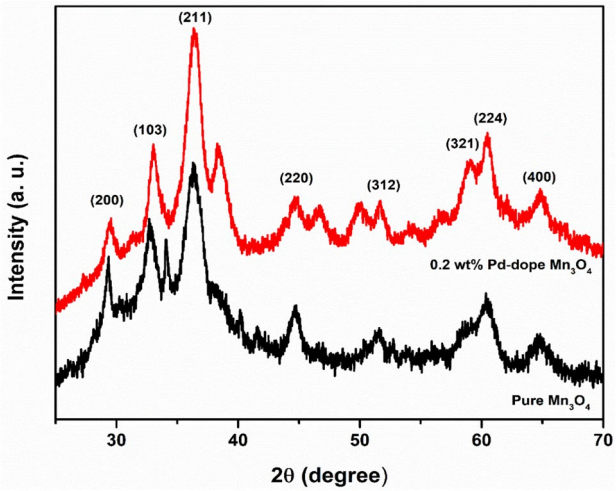

Figure 3. XRD spectra of pure and Pd-doped Mn_3O_4 NPs.

FTIR spectrum of ASAB extract revealed a broad band at ~ 3431.62 cm^{-1}, which corresponds to the OH group[45], alkyl CH stretching (sp^3), and C–O ester group was observed at ~ 2931.95 and ~ 1711.92 cm^{-1}, respectively[48]. A sharp peak at ~ 1611.99 cm^{-1} belongs to –C = C aromatic stretching vibrations and C = O stretching vibrations of proteins denoting amide linkages [45]. The aromatic groups were indicated at ~ 1511.36 cm^{-1}[48], while two separate peaks at ~ 1366.60 cm^{-1}[45] and ~ 1051.25 cm^{-1}[48] denoted the C–O group. These characteristic FTIR spectral peaks suggest for eugenol presence in ASAB extract[48]. The peak at ~ 640 cm^{-1} are attributed to the Mn–O in synthesized nanoparticles[49]. The peaks common to ASAB extract, pure and Pd-doped Mn_3O_4 NPs (~ 3450–3400, ~ 1750–1700, ~ 1650–1600, ~ 1400–1350, and ~ 1050 cm^{-1}) depicted the capping potential of bioactive compounds in phytoextract.

Structural analysis. The XRD confirms the crystalline structure of the prepared manganese oxide NPs with two distinct phases, as shown in Fig. 3. The diffraction peaks of Mn_3O_4 samples at 2θ values of 31.04, 32.36, 36.13, 44.47, 53.83, 58.57, 59.90, and 64.69 matched well with the (200), (103), (211), (220), (312), (321), (224), and (400) crystal planes of Mn_3O_4 phase respectively[50]. The above (hkl) planes correspond to the Hausmannite phase of the Mn_3O_4 crystal structure (JCPDS 24–0734)[51]. The intensity of XRD peaks was decreased in the case of Pd doping, indicating peak shifting towards lower diffraction angles and crystalline lattice expansion[52], suggesting the successful incorporation of Pd in Mn_3O_4. There is no shifting of XRD peaks in the case of Mn_3O_4 NPs, indicating that as-synthesized NPs are comprised of the tetragonal Hausmannite phase[53]. The sharp peaks confirmed the highly crystalline nature of NPs[54]. There were no other peaks in the XRD pattern that demonstrated the phase purity of the produced NPs[55].

The crystallite size of synthesized NPs were calculated by Scherrer's formula at a extremely intense peak (Eq. 5), and the values were ~ 32 and ~ 28 nm for pure and Pd-doped Mn_3O_4 NPs, respectively[56,57]. The Pd-doped

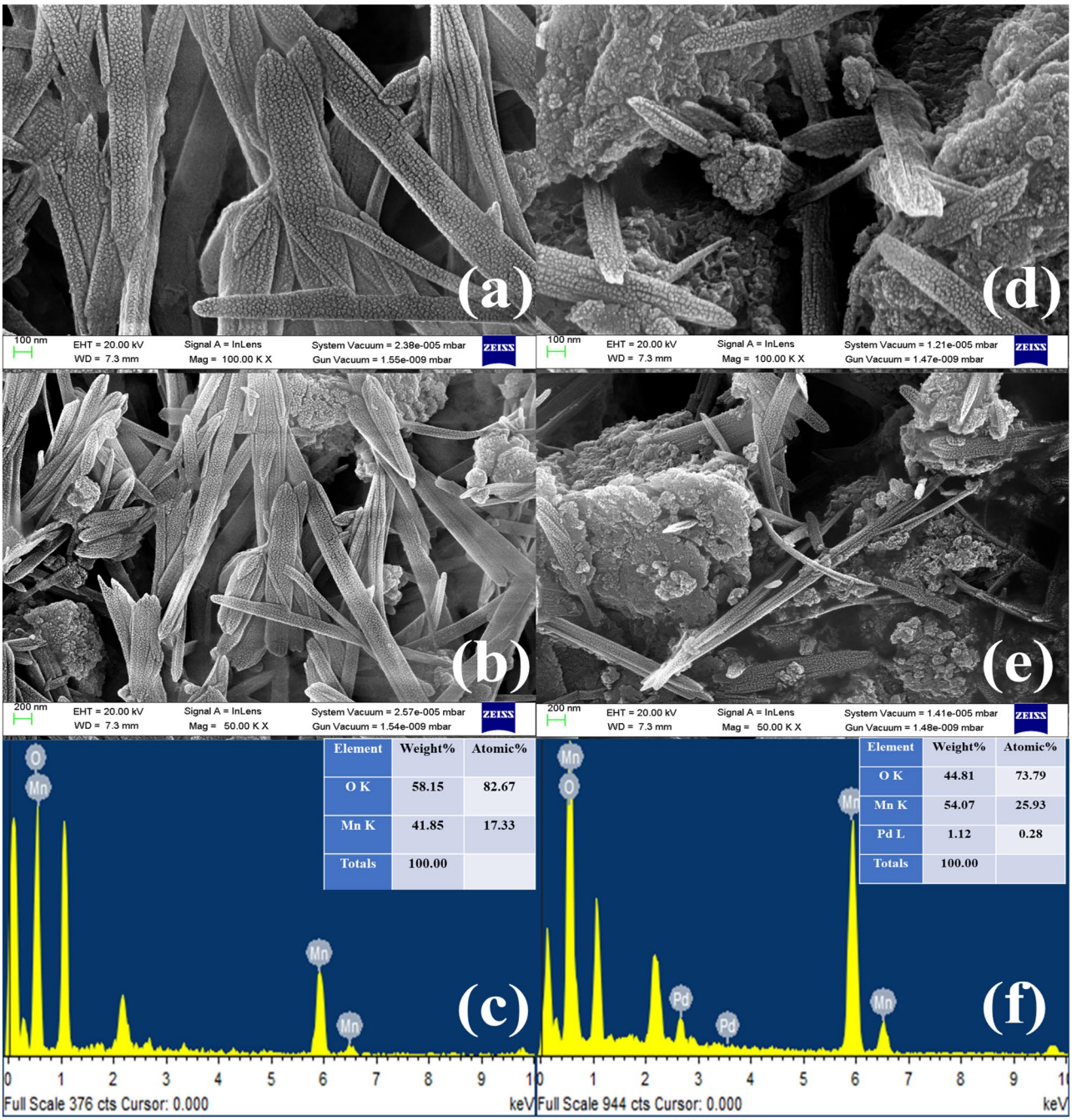

Figure 4. FESEM micrographs, and EDAX spectra of (**a**, **b, c**) pure Mn_3O_4 NPs and (**d, e, f**) Pd-doped Mn_3O_4 NPs.

Mn_3O_4 NPs were smaller than the pure Mn_3O_4 NPs, which could be owing to the fact that ionic radii of Pd (0.137 nm) are much larger than that of Mn (0.082 nm)[58].

$$D = \frac{0.89\lambda}{\beta cos\theta} \tag{5}$$

where D is crystallite size, λ is the wavelength, θ is Bragg's angle, and β is FWHM.

Surface morphology and elemental analysis. The surface morphology of the pure Mn_3O_4 NPs in Fig. 4a, b appeared to be rod-like nanostructures. In contrast, Fig. 4d, e showed the surface of Pd doped-Mn_3O_4 NPs with the likely appearance of nanocorn-like structures. The morphological changes from rod (Mn_3O_4 NPs) to nanocorn-like nanocorn (Pd-doped Mn_3O_4 NPs) could be owing to the decoration of Mn_3O_4 with Pd^{2+}. EDAX analysis revealed Pd, Mn, and O in their suitable stoichiometric proportion, as given in Fig. 4c, f[59].

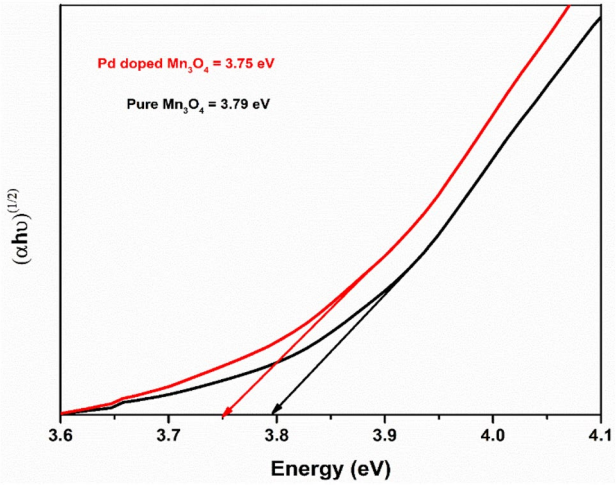

Figure 5. Tauc's plot of pure and Pd-doped Mn_3O_4 NPs.

Optical studies. The absorption spectra of pure and Pd-doped Mn_3O_4 NPs were recorded at room temperature using a UV–visible spectrophotometer. In absorption spectra, the optical absorption edge was shifted to a higher wavelength region with Pd doping; consequently, the red shift was noticed in Pd-doped Mn_3O_4 NPs. The energy band gap of developed NPs was calculated by Tauc's relation (Eq. 6)[60].

$$(\alpha h\nu)^n = B(h\nu - E_g), \tag{6}$$

where α, hν, E_g, and B are the absorption coefficient, photon energy, the band gap energy, and constant, respectively. The value of index 'n' calculated from Tauc's Plot was 2 (Fig. 5). The estimated band gap was ~ 3.79 and ~ 3.75 eV for pure and Pd-doped Mn_3O_4 NPs, respectively, which is in agreement with the previous reports for Mn_3O_4 NPs[61]. It was noticed that the band gap decreased in Pd-doped Mn_3O_4 NPs, compared to pure Mn_3O_4 NPs. A red shift was observed in the band gap of Pd-doped Mn_3O_4 NPs. This may be due to intermediate levels forming between the CB and VB of the host Mn_3O_4 matrix[62,63]. Pd atoms act as an accepter to decrease the band gap of Mn_3O_4 NPs[64,65]. Therefore, variation in the energy band gap of Mn_3O_4 NPs by Pd doping may have applications in photocatalytic activity[66].

Electronic states and elemental composition analysis. The oxidation states of Pd-doped Mn_3O_4 NPs were determined by XPS analysis[67]. The survey spectrum (Fig. 6a) revealed the presence of Pd, Mn, and O, confirming their existence in the product, i.e., Pd-doped Mn_3O_4 NPs. Further analysis of the Pd 3d spectrum showed a doublet feature[68], providing evidence of Pd species' presence in the material. The peaks observed at 332.17 eV and 335.56 eV in the Pd $3d_{5/2}$ region, along with 340.57 eV and 344.58 eV in the Pd $3d_{3/2}$ region, corresponded to Pd (II) and Pd (IV) states[68]. Moving on to the Mn 2p core-level spectrum, two distinct peaks were observed at binding energies of 654.94 eV, 653.56 eV and 643.53 eV, 642.13 eV for pure and Pd-doped Mn_3O_4 nanocorns, respectively. These peaks were associated with Mn $2p_{1/2}$ and Mn $2p_{3/2}$ in Mn_3O_4 NPs and indicating a spin-orbital splitting of 11.4 eV (Fig. 6b)[69,70]. Additionally, the O1s spectrum peaked at 529.68 eV for pure Mn_3O_4 NPs and 532.89 eV for Pd-doped Mn_3O_4 NPs (Fig. 6d)[70]. This peak confirmed the presence of oxygen in both materials. The XPS analysis provided conclusive evidence that the prepared manganese oxide material was indeed Pd-doped Mn_3O_4 NPs, with the oxidation states of Pd (II) and Pd (IV) and specific Mn 2p states characteristic of Mn_3O_4.

Transmission electron microscopy analysis. The TEM micrograph of the green synthesized Mn_3O_4 NPs in Fig. 7a shows that the Mn_3O_4 NPs were composed of nearly uniform types of particles. The SAED patterns of Mn_3O_4 NPs in Fig. 7b displayed bright rings with some bright spots, suggesting the high crystallinity of the materials[71]. Figure 7c represents the high-resolution TEM images of the Pd-doped Mn_3O_4 NPs, and the magnified calibrated lattice fringes of Mn_3O_4 NPs for the crystal plane of (103) and (211) revealed an interplanar spacing (d-spacing) of 2.7 and 2.4 Å in Fig. 7d. These planes were also observed in the XRD analysis, and the reduction of the d-spacing of these planes is in good agreement with the shifting of the XRD peaks. Therefore, these findings indicate the successful formation of Pd-doped Mn_3O_4 NPs, which was also consistent with the XRD patterns[72,73].

Raman Spectroscopy analysis. Figure 8 presents the Raman spectra of pure and Pd-doped Mn_3O_4 NPs. Two characteristic peaks at ~ 629 and ~ 630 cm^{-1} were observed, corresponding to the skeletal vibrations for pure and Pd-doped samples, respectively. The strongest peaks at ~ 629 and ~ 630 cm^{-1} are consistent with the reported data[74] for both materials. These sharp peaks can be assigned to the A1g mode, representing the Mn–O breathing vibration of divalent manganese ions in tetrahedral coordination. This mode is a characteristic feature

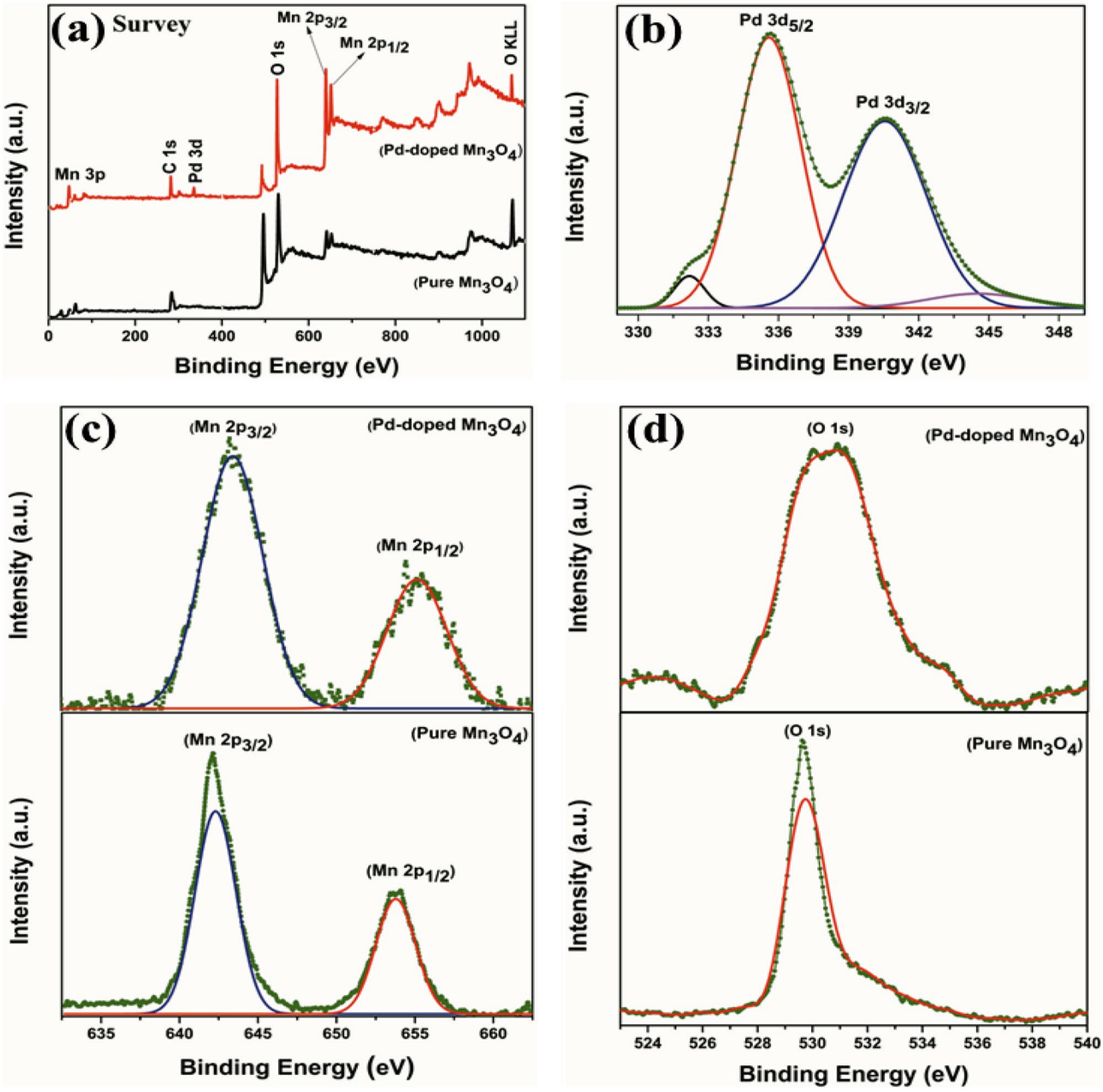

Figure 6. (**a**) The full XPS survey graph of pure and Pd–doped Mn_3O_4; (**b**) Pd 3d (**c**) Mn 2p and (**d**) O 1 s.

of Hausmannite[75,76]. The comparison of the Raman spectra between pure and Pd-doped Mn_3O_4 NPs reveals similarities in the characteristic peaks, indicating that the introduction of Pd did not significantly alter the skeletal vibrations and Mn–O breathing vibrations in the tetrahedral coordination. The Raman spectra analysis of pure and Pd-doped Mn_3O_4 NPs confirmed the presence of specific vibrational modes and provides key insights into the structural properties of these materials. The similarities in the Raman spectra between pure and Pd-doped samples suggested that the Pd-doping did not cause significant changes in the observed vibrational features.

Zeta potential studies. A particle's surface potential substantially impacts its dispersion stability[77], which may also influence its bactericidal potential[78]. Without proper surfactants or capping agents, nanoparticles tend to agglomerate, and their surface area-to-volume ratio decreases due to their increased size[79]. The zeta potential studies allow us to investigate nanoparticles' surface charge and stability in colloidal solutions[80] (Fig. 9). The surface charge of NPs can be influenced by the charged dopants[77], which is also observed in the present study. We have obtained highly stable NPs (ZP > 30 mV)[81], with recorded values of -33.2 ± 0.404 and -36.6 ± 1.74 mV for pure and Pd-doped Mn_3O_4, respectively. The NPs with greater ZP values (negative or positive) prevent agglomeration via electrostatic repulsion, hence conferring stability[80].

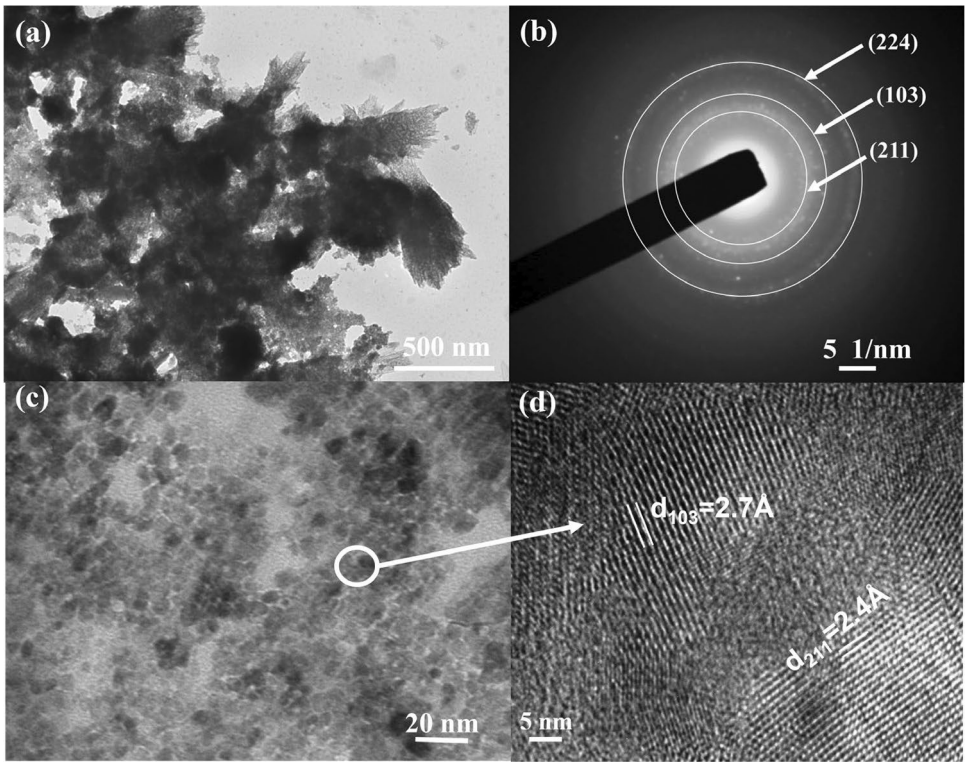

Figure 7. Electron micrographs showing Pd-doped Mn_3O_4 NPs,: (**a**) TEM image, (**b**) SAED pattern, (**c**) HRTEM image, and (**d**) interplanar lattice spacing.

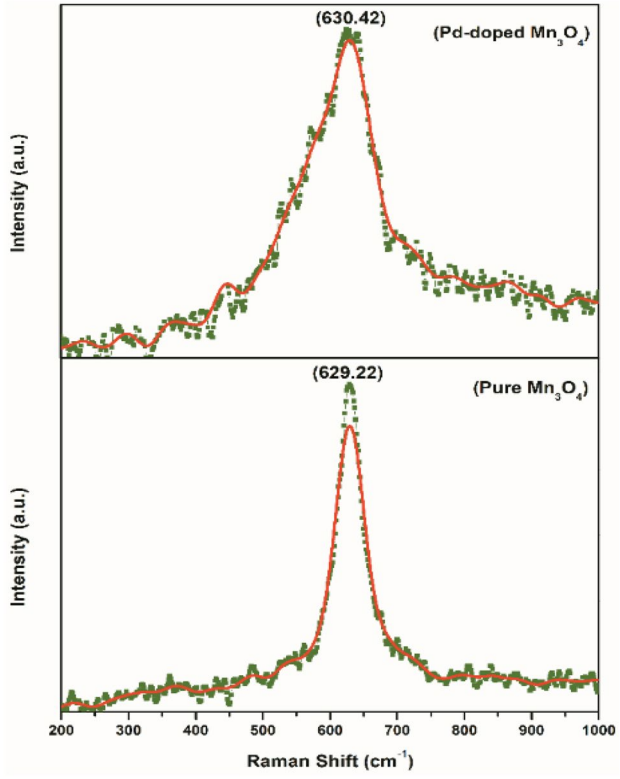

Figure 8. Raman spectra of pure and Pd-doped Mn_3O_4 nanoparticles.

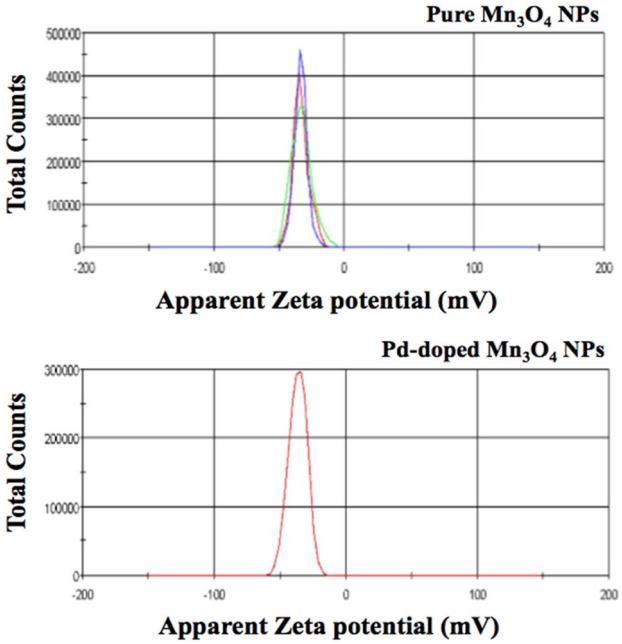

Figure 9. Zeta potential of pure and Pd-doped Mn_3O_4 NPs.

Antifungal activity

The developed NPs showed mycelium growth inhibition in a dose-dependent manner. In the case of Mn_3O_4, NPs, we have observed maximum antifungal activity at 1000-ppm concentration with over 50% inhibitions in the growth of S. sclerotiorum and C. gloeosporioides was recorded at 500 ppm dose (Fig. 10). Overall, S. sclerotiorum exhibited higher sensitivity to the Mn_3O_4 NPs treatment than C. gloeosporioides. The inhibition of mycelial growth in the case of Pd-doped Mn_3O_4 NPs was higher than pure Mn_3O_4 NPs against both fungal strains (Fig. 11). This could be due to the significant modification in structural properties of Mn_3O_4 NPs as a result of Pd doping, such as the reduction in crystallite size and nanocorn-like morphology. At 1000 ppm concentration, Pd-doped Mn_3O_4 NPs caused ~ 92% and ~ 72% growth inhibition of *S. sclerotiorum* and *C. gloeosporioides*, respectively. Interestingly, *C. gloeosporioides* was more sensitive to Pd-doped Mn_3O_4 NPs treatment, specifically at lower doses, and showed ~ 65%, ~ 23%, and ~ 10% higher inhibition compared to pure Mn_3O_4 NPs at 500, 100, and 10 ppm concentration, respectively. The Pd-doped Mn_3O_4 NPs at 1000 ppm showed antifungal activity comparable to those of positive control (2 mg/ml of carbendazim + mancozeb; commercial chemical grade fungicide formulation). Hence, doping Mn_3O_4 NPs with Pd favoured their antifungal potential[66], which is highly explicitly recommended in the case of *C. gloeosporioides* to decrease the effective dose. Overall, the bioinspired fabrication of nanocorn-like Pd doped Mn_3O_4 NPs can be used as an effective antifungal nano-pesticide against different necrotrophic and hemibiotrophic phytopathogens, known for causing enormous loss to agricultural food crops globally.

Antibacterial activity

The antibacterial activity of pure and Pd-doped Mn_3O_4 NPs was also investigated against *E. faecalis* to establish their broad spectrum of antimicrobial potential, in terms of pathogen diversity, i.e., phytopathogens and animal pathogens. As stated earlier, *E. faecalis* is a well-known human pathogen known for hospital acquired infections. This bacterium colonizes the intestine of animals including humans, and its presence in waterbodies is an indicative of fecal contamination. The resistance of *E. faecalis* against various antibiotics necessitated the search of novel materials possessing significant antibacterial potential against such nosocomial pathogens. In the present work, both pure and Pd-doped Mn_3O_4 NPs showed dose-dependent increment in ZOI (Fig. 12). The ZOI values showed effect of Pd doping on improving antibacterial activity of Mn_3O_4 NPs. When compared to pure Mn_3O_4 NPs, Pd doping showed ~ 14%, ~ 17%, and ~ 16% higher ZOI values at 50, 100, and 200 ppm doses of Mn_3O_4 NPs respectively.

Mechanism of antimicrobial activity of Pd-doped Mn_3O_4 NPs

The plausible routes of inducing antimicrobial activity by Pd-doped Mn_3O_4 NPs are illustrated in Fig. 13[36,66,82]. The NPs in fungal cells usually gain entry via diffusion and endocytosis[83] and may cause growth inhibition through multiple actions such as DNA damage, protein denaturation, breakdown of the cell wall and cell membrane, ROS-mediated lipid peroxidation, ribosome disassembly, denaturation of enzymes, perforations in the cell wall and cell membrane, mitochondrial damage, release of cytochrome-c from mitochondria to cytosol, and increase levels of metacaspase and promotes cell death[36]. Similar effects have been proposed in the case of bacterial cells where NPs can cause protein and enzyme denaturation, damage to chromosomal and plasmid

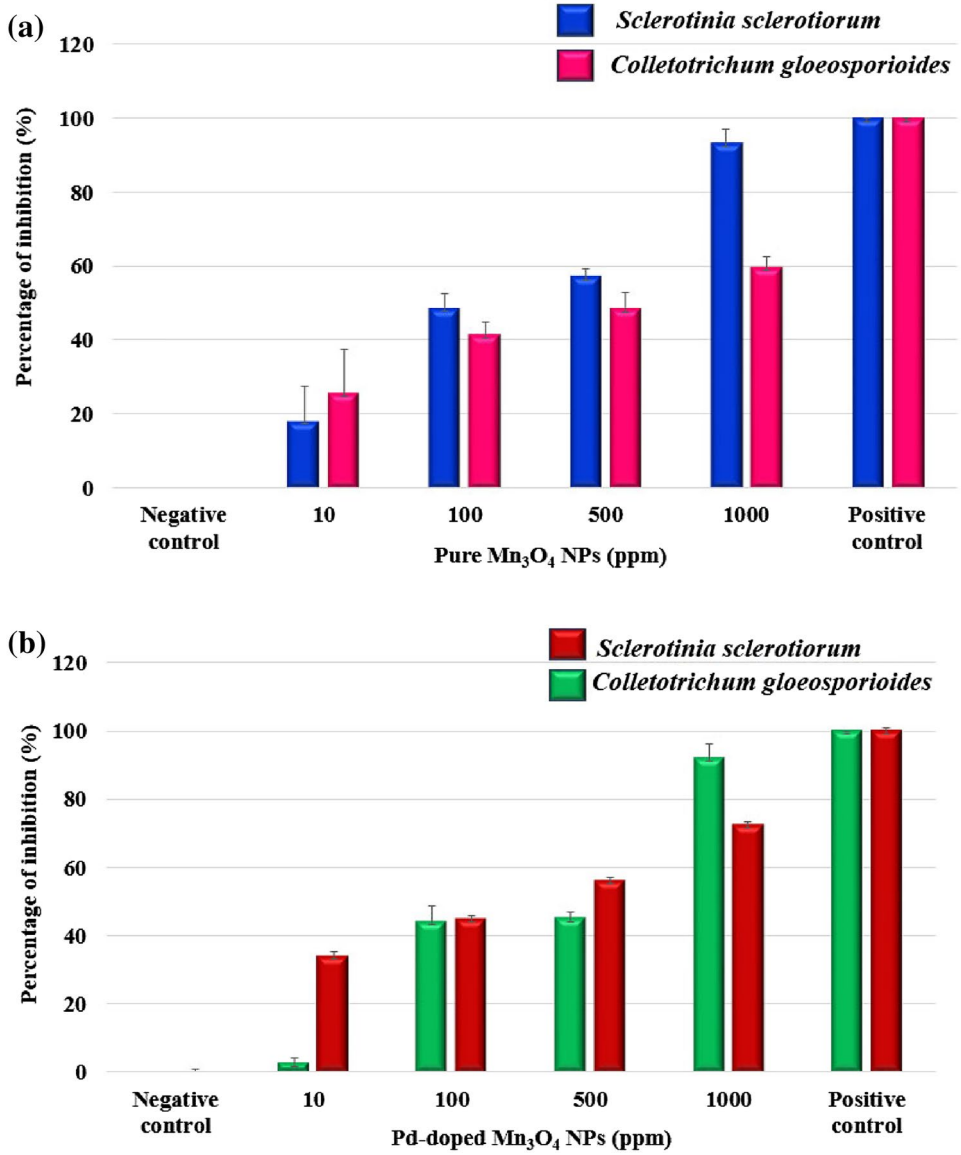

Figure 10. Effect of (**a**) pure Mn_3O_4 NPs, and (**b**) Pd- doped Mn_3O_4 NPs on growth of *S. sclerotiorum*, and *C. gloeosporioides*.

DNA, ribosomal depolymerization, interference in ETC, the release of cellular contents, disruption of the cell membrane, etc.[84,85].

In general, NPs have direct and indirect effects on microbial cells. The direct damage occurs via the electrostatic interaction of NPs with cell membrane resulting in membrane depolarization and loss of membrane integrity leading to the disruption in ETC and cell lysis[39,86]. The indirect damage to microbial cells is reported via ROS generation (Eqs. 7, 8, 9, 10, 11, 12)[39,87]. The doping in pure nanomaterial leads to lattice defects (alters band gap), causing overlapping of Fermi levels, variation in cellular redox potential, promotes ROS generation (Fig. 14) and can impart enhanced antimicrobial properties[39], which was observed in the present study as well, where Pd-doped Mn_3O_4 NPs showed higher antifungal and antibacterial activity compared to pure NPs. In addition, doping can improve the binding capacity and cellular internalization ability of NPs. NPs generate ROS outside the cellular environment or can produce it inside the cell due to interference in ETC[39]. The oxygen molecules that are not reduced in the water get oxidized into free radicals (such as superoxide anion, singlet oxygen, or hydroxyl radicals) in mitochondria (Eqs. 7, 8, 9, 10, 11, 12)[39,88]. ROS causes alteration in protein structures, oxidative stress, lipid peroxidation, and DNA damage[88].

$$\text{Pd-doped } Mn_3O_4 + \text{ hv} \rightarrow e^- + h^+ \tag{7}$$

$$h^+ H_2O \rightarrow {}^{\bullet}OH + H^+ \tag{8}$$

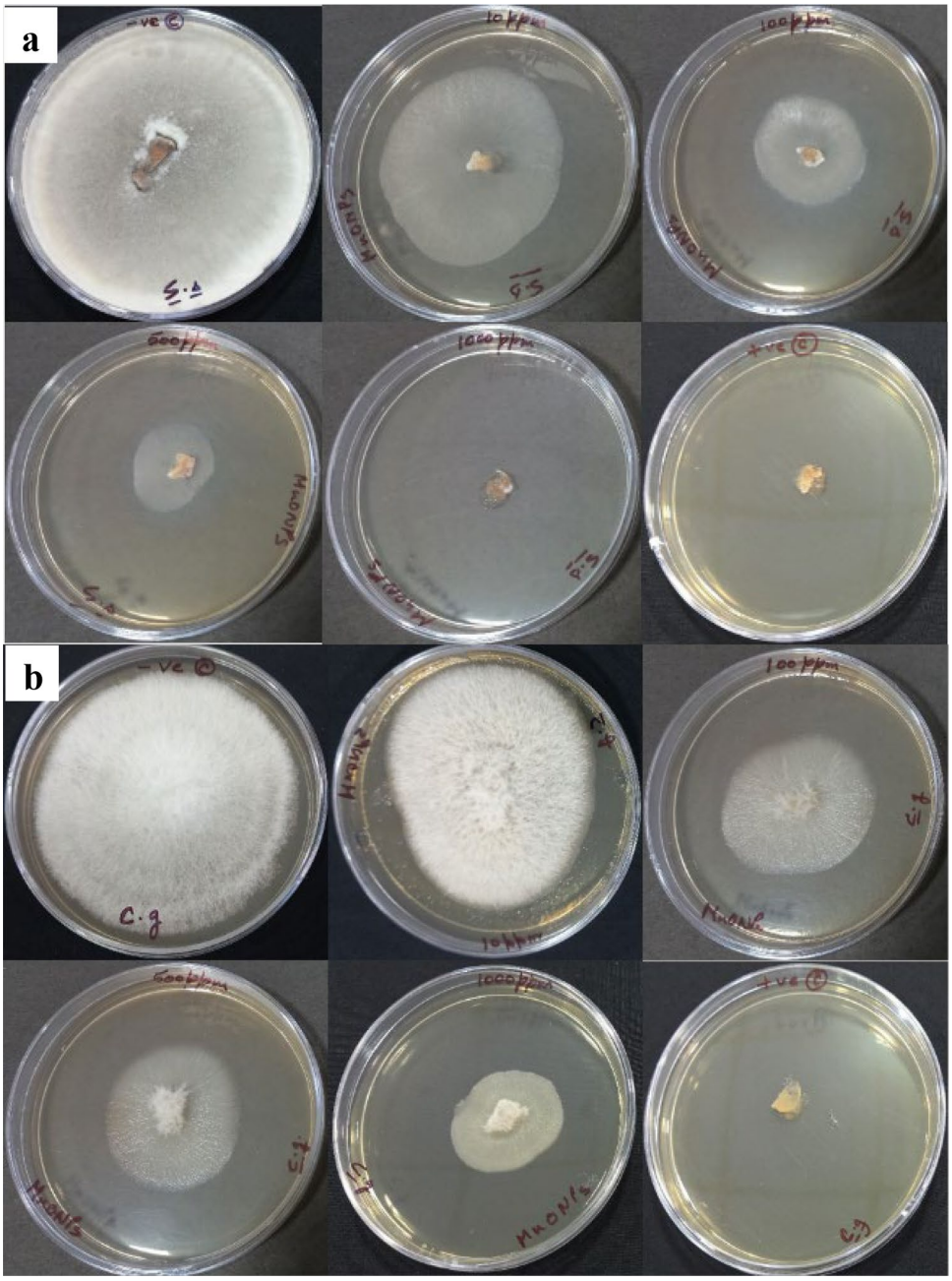

Figure 11. Antifungal activity of pure and Pd-doped Mn_3O_4 NPs against (**a**) *S. sclerotiorum*, and (**b**) *C. gloeosporioides*.

$$e^- + O_2 \rightarrow {}^{\bullet}O_2^- \tag{9}$$

$${}^{\bullet}O_2^- + H^+ \rightarrow HO_2^{\bullet} \tag{10}$$

$$HO_2^{\bullet} + H^+ + e^- \rightarrow H_2O_2 \tag{11}$$

$$H_2O_2 + e^- \rightarrow {}^{\bullet}OH + HO^- \tag{12}$$

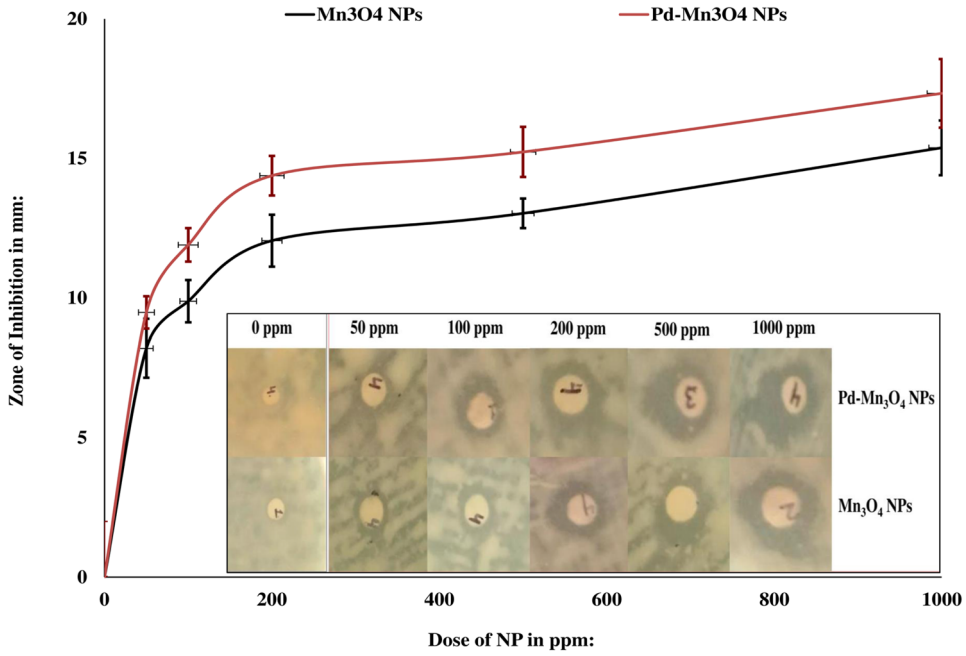

Figure 12. Antibacterial activity of pure and Pd-doped Mn_3O_4 NPs against *E. faecalis*.

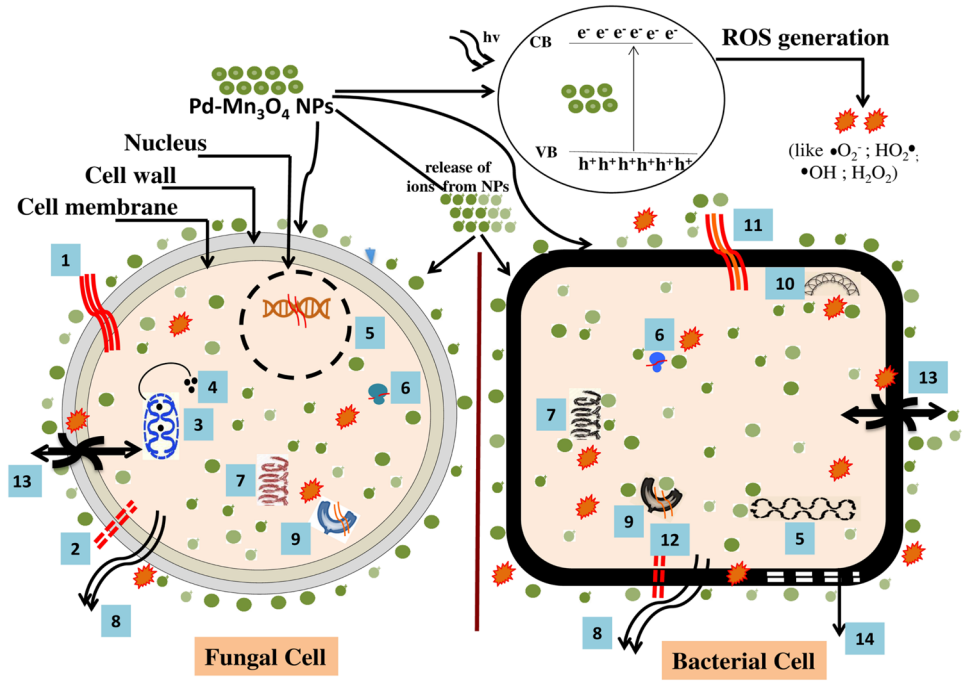

Figure 13. Schematic representation highligting plausible mechanisms involved in antimicrobial action of Pd-doped Mn_3O_4 NPs (1. breakdown of cell wall and cell membrane; 2. perforations in cell wall and cell membrane; 3. mitochondrial damage; 4. release of cytochrome-c from mitochondria to cytosol, increase levels of metacaspase and promotes cell death; 5. chromosomal DNA damage; 6. ribosome disassembly; 7. Protein damage; 8. release of cellular contents; 9. denaturation of enzymes; 10. plasmid DNA damage; 11. disruption of cell membrane; 12. perforation in cell membrane; 13. interference in ETC and damage to protein-efflux pump; 14. destruction of membranous proteins; CB = conduction band, VB = valance band; ROS: reactive oxygen species).

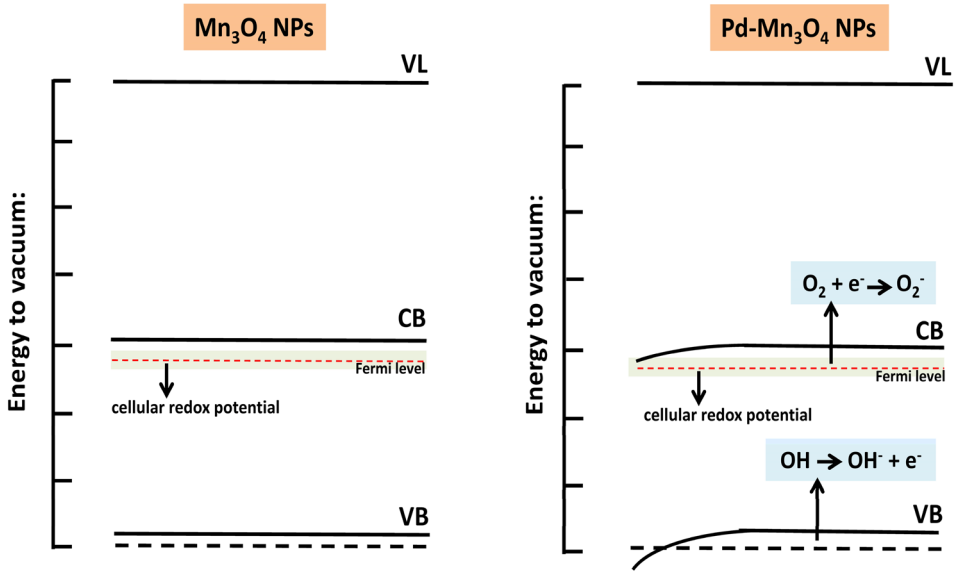

Figure 14. Effect of doping on Fermi levels leading to ROS generation (VL = vacuum level, CB = conduction band, VB = valance band) (conceptualized and redrawn from[39]).

Conclusion

The present investigation demonstrates a successful green chemistry approach to synthesis pure and Pd-doped Mn_3O_4 NPs via utilizing an aqueous extract of *S. aromaticum* buds. Adding Pd in Mn_3O_4 resulted in significant changes to their structural attributes, including morphology, crystallite size, and lattice defects. The Pd-doped Mn_3O_4 NPs exhibited antimicrobial activity in a dose-dependent manner and provides higher inhibitory effects than pure Mn_3O_4 NPs against *S. sclerotiorum*, *C. gloeosporioides*, and *E. faecalis*. The outcome of this study provides a novel, cost-effective method to develop Pd-doped Mn_3O_4 based nanomaterials for highly effective antimicrobial applications against tested microbial pathogens. This breakthrough opens up new possibilities in the area of green nanotechnology to develop sustainable and multifaceted antimicrobial agents.

Data availability

All data generated or analyzed during this study are included within the article.

Received: 26 May 2023; Accepted: 17 August 2023
Published online: 28 August 2023

References

1. Alshora, D. H., Ibrahim, M. A., Alanazi, F. K. (2016). Nanotechnology from particle size reduction to enhancing aqueous solubility. In *Surface Chemistry of Nanobiomaterials*. Elsevier, pp. 163–191. https://doi.org/10.1016/B978-0-323-42861-3.00006-6.
2. Al-Zahrani, F. A. M. *et al.* Green synthesis and antibacterial activity of Ag/Fe_2O_3 nanocomposite using buddleja lindleyana extract. *Bioengineering* **9**, 452. https://doi.org/10.3390/bioengineering9090452 (2022).
3. Salem, S. S. A mini review on green nanotechnology and its development in biological effects. *Arch Microbiol* **205**, 128. https://doi.org/10.1007/s00203-023-03467-2 (2023).
4. Salem, S. S. & Fouda, A. Green synthesis of metallic nanoparticles and their prospective biotechnological applications: An overview. *Biol Trace Elem Res* **199**, 344–370. https://doi.org/10.1007/s12011-020-02138-3 (2021).
5. Asghari F, Jahanshiri Z, Imani M, et al (2016) Antifungal nanomaterials. In *Nanobiomaterials in Antimicrobial Therapy*. Elsevier, pp. 343–383. https://doi.org/10.1016/B978-0-323-42864-4.00010-5.
6. Ali, Md. A. *et al.* Advancements in plant and microbe-based synthesis of metallic nanoparticles and their antimicrobial activity against plant pathogens. *Nanomaterials* **10**, 1146. https://doi.org/10.3390/nano10061146 (2020).
7. Zhang, S. *et al.* Antimicrobial properties of metal nanoparticles and their oxide materials and their applications in oral biology. *J. Nanomater.* **2022**, 1–18. https://doi.org/10.1155/2022/2063265 (2022).
8. Abdelghany, T. M. *et al.* Phytofabrication of zinc oxide nanoparticles with advanced characterization and its antioxidant, anticancer, and antimicrobial activity against pathogenic microorganisms. *Biomass Conv Bioref* **13**, 417–430. https://doi.org/10.1007/s13399-022-03412-1 (2023).
9. Salem, S. S. Bio-fabrication of selenium nanoparticles using Baker's yeast extract and its antimicrobial efficacy on food borne pathogens. *Appl Biochem Biotechnol* **194**, 1898–1910. https://doi.org/10.1007/s12010-022-03809-8 (2022).
10. Shehabeldine, A. M. *et al.* Potential antimicrobial and antibiofilm properties of copper oxide nanoparticles: Time-kill kinetic essay and ultrastructure of pathogenic bacterial cells. *Appl Biochem Biotechnol* **195**, 467–485. https://doi.org/10.1007/s12010-022-04120-2 (2023).
11. Soliman, M. K. Y., Salem, S. S., Abu-Elghait, M. & Azab, M. S. Biosynthesis of silver and gold nanoparticles and their efficacy towards antibacterial, antibiofilm, cytotoxicity, and antioxidant activities. *Appl Biochem Biotechnol* **195**, 1158–1183. https://doi.org/10.1007/s12010-022-04199-7 (2023).
12. Vikal, S., Gautam, Y., Kumar, A., Kumar, A., Singh, N., Singh, H., Singh, B. (2022). Effect of silver (Ag) doping on structural, optical and antimicrobial properties of copper oxide (CuO) nanostructures. *Nano Express 4*(2023), 025004. https://doi.org/10.1088/2632-959X/acdc41.

13. Alqarni, L. S., Alghamdi, M. D., Alshahrani, A. A. & Nassar, A. M. Green nanotechnology: Recent research on bioresource-based nanoparticle synthesis and applications. *J. Chem.* **2022**, 1–31. https://doi.org/10.1155/2022/4030999 (2022).
14. Abdelmoneim, H. E. M. *et al.* Multiple applications of CdS/TiO_2 nanocomposites synthesized via microwave-assisted sol–gel. *J Clust Sci* **33**, 1119–1128. https://doi.org/10.1007/s10876-021-02041-4 (2022).
15. Mohamed, A. A., Abu-Elghait, M., Ahmed, N. E. & Salem, S. S. Eco-friendly mycogenic synthesis of ZnO and CuO nanoparticles for in vitro antibacterial, antibiofilm and antifungal applications. *Biol Trace Elem Res* **199**, 2800–2801. https://doi.org/10.1007/s12011-020-02391-6 (2021).
16. Said, A., Abu-Elghait, M., Atta, H. M. & Salem, S. S. Antibacterial activity of green synthesized silver nanoparticles using lawsonia inermis against common pathogens from urinary tract infection. *Appl Biochem Biotechnol* https://doi.org/10.1007/s12010-023-04482-1 (2023).
17. Salem, S. S. Baker's yeast-mediated silver nanoparticles: characterisation and antimicrobial biogenic tool for suppressing pathogenic microbes. *BioNanoSci* **12**, 1220–1229. https://doi.org/10.1007/s12668-022-01026-5 (2022).
18. Soliman, M. K. Y., Abu-Elghait, M., Salem, S. S. & Azab, M. S. Multifunctional properties of silver and gold nanoparticles synthesis by *Fusarium pseudonygamai*. *Biomass Conv Bioref* https://doi.org/10.1007/s13399-022-03507-9 (2022).
19. Jeyabharathi, S. *et al.* Self-assembled hollow ZnO nano and micro donut shape by starch and its antimicrobial potentials. *Mater Lett.* **275**, 128128. https://doi.org/10.1016/j.matlet.2020.128128 (2020).
20. Kalam, A. *et al.* Antimicrobial properties of silver nanoparticles prepared by *Acacia etbaica* (Schweinf.) valve extract. *Mater. Lett.* **300**, 130233. https://doi.org/10.1016/j.matlet.2021.130233 (2021).
21. Parvathy, S., Subramanian, P., Arun Karthick, S. & Subbaiya, R. The structural, optical, antimicrobial and anticancer properties of biocompatible astaxanthin coated ZnO and CeO_2 nanoparticles. *Mater. Lett.* **312**, 131669. https://doi.org/10.1016/j.matlet.2022.131669 (2022).
22. Parvathy, S., Manjula, G., Balachandar, R. & Subbaiya, R. Green synthesis and characterization of cerium oxide nanoparticles from *Artabotrys hexapetalus* leaf extract and its antibacterial and anticancer properties. *Materials Letters* **314**, 131811. https://doi.org/10.1016/j.matlet.2022.131811 (2022).
23. Bhardwaj et al. (2020). https://doi.org/10.1016/10.34172/apb.2020.067.
24. Hoseinpour, V. & Ghaemi, N. Green synthesis of manganese nanoparticles: Applications and future perspective—a review. *J. Photochem. Photobiol. B* **189**, 234–243. https://doi.org/10.1016/j.jphotobiol.2018.10.022 (2018).
25. Suresh, K. C. & Balamurugan, A. Evaluation of structural, optical, and morphological properties of nickel oxide nanoparticles for multi-functional applications. *Inorganic Nano-Metal Chem.* **51**, 296–301. https://doi.org/10.1080/24701556.2020.1770793 (2021).
26. Alavi, M., Karimi, N. & Valadbeigi, T. Antibacterial, antibiofilm, antiquorum sensing, antimotility, and antioxidant activities of green fabricated Ag, Cu, TiO_2, ZnO, and Fe_3O_4 NPs via *Protoparmeliopsis muralis* lichen aqueous extract against multi-drug-resistant bacteria. *ACS Biomater Sci Eng* **5**, 4228–4243. https://doi.org/10.1021/acsbiomaterials.9b00274 (2019).
27. Bao, Y. *et al.* Plant-extract-mediated synthesis of metal nanoparticles. *J. Chem.* **2021**, 1–14. https://doi.org/10.1155/2021/6562687 (2021).
28. Kumar, B. Green synthesis of gold, silver, and iron nanoparticles for the degradation of organic pollutants in wastewater. *J Compos Sci* **5**, 219. https://doi.org/10.3390/jcs5080219 (2021).
29. Nicolas, J. *et al.* Design, functionalization strategies and biomedical applications of targeted biodegradable/biocompatible polymer-based nanocarriers for drug delivery. *Chem Soc Rev* **42**, 1147–1235. https://doi.org/10.1039/C2CS35265F (2013).
30. Veeramani, H. *et al.* Low-temperature green synthesis of multivalent manganese oxide nanowires. *ACS Sustain. Chem. Eng.* **1**, 1070–1074. https://doi.org/10.1021/sc400129n (2013).
31. Prasad, A. S. Green synthesis of nanocrystalline manganese (II, III) oxide. *Mater. Sci. Semicond. Process.* **71**, 342–347. https://doi.org/10.1016/j.mssp.2017.08.020 (2017).
32. Fei, J. B. *et al.* Controlled preparation of MnO_2 hierarchical hollow nanostructures and their application in water treatment. *Adv Mater* **20**, 452–456. https://doi.org/10.1002/adma.200701231 (2008).
33. Gong, Y. *et al.* Sclerotinia sclerotiorum SsCut1 modulates virulence and cutinase activity. *JoF* **8**, 526. https://doi.org/10.3390/jof8050526 (2022).
34. Sharma, M. & Kulshrestha, S. Colletotrichum gloeosporioides: An anthracnose causing pathogen of fruits and vegetables. *Biosci. Biotechnol. Res. Asia* **12**, 1233–1246. https://doi.org/10.13005/bbra/1776 (2015).
35. Siddiqui Y, Ali A (2014) Colletotrichum gloeosporioides (Anthracnose). In *Postharvest Decay*. Elsevier, pp. 337–371. https://doi.org/10.1016/B978-0-12-411552-1.00011-9.
36. Dubin, K., & Pamer, E. G. (2017) Enterococci and their interactions with the intestinal microbiome. *Microbiol. Spectr.* **5**:5.6.01. https://doi.org/10.1128/microbiolspec.BAD-0014-2016.
37. Olawale, K., Fadiora, S., Taiwo, S. (2011). Prevalence of hospital acquired enterococci infections in two primary-care hospitals in Osogbo, Southwestern Nigeria. *Afr. J. Infect. Dis.* **5**. https://doi.org/10.4314/ajid.v5i2.66513.
38. Gnana Sundara Raj, B., Asiri, A. M., Wu, J. J. & Anandan, S. Synthesis of Mn_3O_4 nanoparticles via chemical precipitation approach for supercapacitor application. *J. Alloy. Compd.* **636**, 234–240. https://doi.org/10.1016/j.jallcom.2015.02.164 (2015).
39. Patra, T. *et al.* Effect of calcination temperature on morphology and phase transformation of MnO_2 nanoparticles: A step towards green synthesis for reactive dye adsorption. *Chemosphere* **288**, 132472. https://doi.org/10.1016/j.chemosphere.2021.132472 (2022).
40. Revathy, J. S., Priya, N. S. C., Sandhya, K. & Rajendran, D. N. Structural and optical studies of cerium doped gadolinium oxide phosphor. *Bull Mater Sci* **44**, 13. https://doi.org/10.1007/s12034-020-02299-w (2021).
41. Amer, A. A., Reda, S. M., Mousa, M. A. & Mohamed, M. M. Mn_3O_4/graphene nanocomposites: Outstanding performances as highly efficient photocatalysts and microwave absorbers. *RSC Adv.* **7**, 826–839. https://doi.org/10.1039/C6RA24815B (2017).
42. Arniati, A., Pratama, M., Baits, M., & Tahir, M. (2022). Determination of total phenolic levels of ethyl acetate fraction of clove leaves (*Syzygium aromaticum* (L.) Merr). *Pharmaceut. Rep.*, **1**(2).
43. Jimoh, S. O., Arowolo, L. A. & Alabi, K. A. Phytochemical screening and antimicrobial evaluation of *Syzygium aromaticum* extract and essential oil. *Int. J. Curr. Microbiol. Appl. Sci.* **6**, 4557–4567. https://doi.org/10.20546/ijcmas.2017.607.476 (2017).
44. Lone, Z. A. & Jain, N. K. Phytochemical analysis of clove (*Syzygium aromaticum*) dried flower buds extract and its therapeutic importance. *J. Drug Deliv. Therap.* **12**, 87–92. https://doi.org/10.22270/jddt.v12i4-S.5628 (2022).
45. Rajesh, K. M. *et al.* Assisted green synthesis of copper nanoparticles using *Syzygium aromaticum* bud extract: Physical, optical and antimicrobial properties. *Optik* **154**, 593–600. https://doi.org/10.1016/j.ijleo.2017.10.074 (2018).
46. Jardón-Romero, E. A. *et al.* Antimicrobial activity of biogenic silver nanoparticles from *Syzygium aromaticum* against the five most common microorganisms in the oral cavity. *Antibiotics* **11**, 834. https://doi.org/10.3390/antibiotics11070834 (2022).
47. Lakshmeesha, T. R. *et al.* Biofabrication of zinc oxide nanoparticles with *Syzygium aromaticum* flower buds extract and finding its novel application in controlling the growth and mycotoxins of *Fusarium graminearum*. *Front Microbiol* **10**, 1244. https://doi.org/10.3389/fmicb.2019.01244 (2019).
48. Parthipan, P., AlSalhi, M. S., Devanesan, S. & Rajasekar, A. Evaluation of *Syzygium aromaticum* aqueous extract as an eco-friendly inhibitor for microbiologically influenced corrosion of carbon steel in oil reservoir environment. *Bioprocess Biosyst Eng* **44**, 1441–1452. https://doi.org/10.1007/s00449-021-02524-8 (2021).
49. Atique Ullah, A. K. M. *et al.* Oxidative degradation of methylene blue using Mn_3O_4 nanoparticles. *Water Conserv Sci Eng* **1**, 249–256. https://doi.org/10.1007/s41101-017-0017-3 (2017).

50. Li, Q. *et al.* Correlation between particle size/domain structure and magnetic properties of highly crystalline Fe_3O_4 nanoparticles. *Sci Rep* **7**, 9894. https://doi.org/10.1038/s41598-017-09897-5 (2017).
51. Kadam, A. *et al.* Template free synthesis of ZnO/Ag_2O nanocomposites as a highly efficient visible active photocatalyst for detoxification of methyl orange. *J. Photochem. Photobiol. B* **154**, 24–33. https://doi.org/10.1016/j.jphotobiol.2015.11.007 (2016).
52. Muñoz-Fernandez, L., Sierra-Fernandez, A., Milošević, O. & Rabanal, M. E. Solvothermal synthesis of Ag/ZnO and Pt/ZnO nanocomposites and comparison of their photocatalytic behaviors on dyes degradation. *Adv. Powder Technol.* **27**, 983–993. https://doi.org/10.1016/j.apt.2016.03.021 (2016).
53. Liu, H. *et al.* Microwave-assisted one-pot synthesis of Ag decorated flower-like ZnO composites photocatalysts for dye degradation and NO removal. *Ceram. Int.* **45**, 20133–20140. https://doi.org/10.1016/j.ceramint.2019.06.279 (2019).
54. Zeferino, R. S., Flores, M. B. & Pal, U. Photoluminescence and Raman Scattering in Ag-doped ZnO Nanoparticles. *Journal of Applied Physics* **109**, 014308. https://doi.org/10.1063/1.3530631 (2011).
55. Nie, M. *et al.* Photocatalytic property of silver enhanced Ag/ZnO composite catalyst. *Chem. Phys. Lett.* **768**, 138394. https://doi.org/10.1016/j.cplett.2021.138394 (2021).
56. AL-Jawad, S. M. H., Sabeeh, S. H., Taha, A. A., Jassim, H. A. (2018). Studying structural, morphological and optical properties of nanocrystalline ZnO:Ag films prepared by sol–gel method for antimicrobial activity. *J. Sol-Gel Sci. Technol.* 87:362–371. https://doi.org/10.1007/s10971-018-4724-9.
57. Hosny, N. M. & Dahshan, A. Facile synthesis and optical band gap calculation of Mn_3O_4 nanoparticles. *Mater. Chem. Phys.* **137**, 637–643. https://doi.org/10.1016/j.matchemphys.2012.09.068 (2012).
58. Mallesham, B. *et al.* Crystal chemistry, band-gap red shift, and electrocatalytic activity of iron-doped gallium oxide ceramics. *ACS Omega* **5**, 104–112. https://doi.org/10.1021/acsomega.9b01604 (2020).
59. Kösemen, A. *et al.* Electrochemical growth of Pd doped ZnO nanorods. *J Electrochem Soc* **162**, D142–D146. https://doi.org/10.1149/2.0341504jes (2015).
60. Kumar, S., Singh, V. & Tanwar, A. Structural, morphological, optical and photocatalytic properties of Ag-doped ZnO nanoparticles. *J Mater Sci: Mater Electron* **27**, 2166–2173. https://doi.org/10.1007/s10854-015-4227-1 (2016).
61. Sagadevan, S., Pal, K., Chowdhury, Z. Z. & Hoque, M. E. Structural, dielectric and optical investigation of chemically synthesized Ag-doped ZnO nanoparticles composites. *J Sol–Gel Sci Technol* **83**, 394–404. https://doi.org/10.1007/s10971-017-4418-8 (2017).
62. Slavin, Y. N. & Bach, H. Mechanisms of antifungal properties of metal nanoparticles. *Nanomaterials* **12**, 4470. https://doi.org/10.3390/nano12244470 (2022).
63. Jamil, S. *et al.* Synthesis of saucer shaped manganese oxide nanoparticles by co-precipitation method and the application as fuel additive. *J. Clust. Sci.* **29**, 1099–1106. https://doi.org/10.1007/s10876-018-1428-9 (2018).
64. Oba, M., Oaki, Y. & Imai, H. A microbial-mineralization-inspired approach for synthesis of manganese oxide nanostructures with controlled oxidation states and morphologies. *Adv. Funct. Mater.* **20**, 4279–4286. https://doi.org/10.1002/adfm.201000361 (2010).
65. Gurunathan, S., Lee, A. R. & Kim, J. H. Antifungal effect of nanoparticles against COVID-19 linked black fungus: A perspective on biomedical applications. *IJMS* **23**, 12526. https://doi.org/10.3390/ijms232012526 (2022).
66. Mubeen, B. *et al.* Nanotechnology as a novel approach in combating microbes providing an alternative to antibiotics. *Antibiotics* **10**, 1473. https://doi.org/10.3390/antibiotics10121473 (2021).
67. Gnana Sundara Raj, B., Angulakshmi, R., Baskaran, N., Wu, J. J., Anandan, S., Ashok Kumar, M. Pseudocapacitive performance of Mn_3O_4–SnO_2 hybrid nanoparticles synthesized via ultrasonication approach. *J. Appl. Electrochem.* https://doi.org/10.1007/s10800-020-01421-4.
68. Wang, P. *et al.* PdO/SnO_2 heterostructure for low-temperature detection of CO with fast response and recovery. *RSC Adv.* **9**, 22875. https://doi.org/10.1039/c9ra03171e (2019).
69. Ren, L. *et al.* Magnetic properties of Mn_3O_4 film with a coexistence of two preferential orientations. *J Appl Phys* **116**, 023906 (2014).
70. Jin, R., Liu, H., Guan, Y., Zhou, J. & Li, G. Molten salt synthesis of fuorine-doped Mn_3O_4 nanobelts as anode materials for Li-ion batteries. *Cryst Eng Commun* **17**, 7717–7722 (2015).
71. Acharyya, S. S., Ghosh, S., Sharma, S. K. & Bal, R. Cetyl alcohol mediated fabrication of forest of Ag/Mn_3O_4 nanowhiskers catalyst for the selective oxidation of styrene with molecular oxygen. *RSC Adv.* **5**, 89879–89887 (2015).
72. Chen, X. *et al.* Performance enhancement of asymmetric supercapacitors with bud-like Cu-doped Mn_3O_4 hollow and porous structures on nickel foam as positive electrodes. *RSC Adv.* **8**, 35878–35887 (2018).
73. Sukhdev, A., Challa, M., Narayani, L., Manjunatha, A. S., Deepthi, P. R., Angadi, J. V., Kumar, P. M., Pasha, M. Synthesis, phase transformation, and morphology of hausmannite Mn_3O_4 nanoparticles: Photocatalytic and antibacterial investigations. *Heliyon* **6**, e03245 (2020).
74. Bussamara, R., Melo, W. W. M., Scholten, J. D., Migowski, P., Marin, G., Zapata, M. J. M., Machado, G., Teixeira, S. R., Novak, M., Dupont, J. *Dalton Trans.* **42**, 14473 (2013).
75. Buciuman, F., Patcas, F., Craciun, R., Zahn, D. R. T. *Phys. Chem. Chem. Phys.* **1**, 185 (1999).
76. Moulder, J. F., Stickle, W. F., Sobol, P. E., Bomben, K. D. *Handbook of X-ray Photoelectron Spectroscopy*, Perkin-Elmer Corp., Physical Electronics Division, Eden Prairie, Minnesota, USA (1979).
77. Pinton. A. P., Bulhões, L. O. D. Synthesis, characterization, and photostability of manganese-doped titanium dioxide nanoparticles and the effect of manganese content. *Mater. Res. Express* **6**, 125015. https://doi.org/10.1088/2053-1591/ab533b (2019).
78. Ichimaru, H. *et al.* Gold coating of silver nanoplates for enhanced dispersion stability and efficient antimicrobial activity against intracellular bacteria. *Langmuir* **34**, 10413–10418. https://doi.org/10.1021/acs.langmuir.8b00540 (2018).
79. Ullah, M., Bee, S. & Hamid, A. Surfactant-assisted ball milling: a novel route to novel materials with controlled nanostructure: A review. *Rev. Adv. Mater. Sci.* **37**(2014), 1–14 (2014).
80. İlhan M, Gültekin HE, Rençber S, et al (2022) Aquasomes: A novel platform for drug delivery. In *Systems of Nanovesicular Drug Delivery*. Elsevier, pp. 191–206.
81. Das, P. & Das, M. K. Chapter 4: Production and physicochemical characterization of nanocosmeceuticals. In *Nanocosmeceuticals* (ed. Das, M. K.) 95–138 (Academic Press, 2022).
82. Abebe, B., Zereffa, E. A., Tadesse, A. & Murthy, H. C. A. A review on enhancing the antibacterial activity of ZnO: Mechanisms and microscopic investigation. *Nanoscale Res Lett* **15**, 190. https://doi.org/10.1186/s11671-020-03418-6 (2020).
83. Naik, M. M. *et al.* Multifunctional properties of microwave-assisted bioengineered nickel doped cobalt ferrite nanoparticles. *J Sol-Gel Sci Technol* **91**, 578–595. https://doi.org/10.1007/s10971-019-05048-6 (2019).
84. Singh, A. *et al.* Zinc oxide nanoparticles: a review of their biological synthesis, antimicrobial activity, uptake, translocation and biotransformation in plants. *J Mater Sci* **53**, 185–201. https://doi.org/10.1007/s10853-017-1544-1 (2018).
85. Bhattacharya, P. & Neogi, S. Antibacterial properties of doped nanoparticles. *Rev. Chem. Eng.* **35**, 861–876. https://doi.org/10.1515/revce-2017-0116 (2019).
86. Jin, S.-E. & Jin, H.-E. Antimicrobial activity of zinc oxide nano/microparticles and their combinations against pathogenic microorganisms for biomedical applications: From physicochemical characteristics to pharmacological aspects. *Nanomaterials* **11**, 263. https://doi.org/10.3390/nano11020263 (2021).
87. Navarro-López, D. E., Garcia-Varela, R., Ceballos-Sanchez, O., et al. (2021). Effective antimicrobial activity of ZnO and Yb-doped ZnO nanoparticles against *Staphylococcus aureus* and *Escherichia coli*. *Mater. Sci. Eng.: C* **123**:112004. https://doi.org/10.1016/j.msec.2021.112004.

88. Khalid, A., Ahmad, P., Alharthi, A. I., et al. (2021). Synergistic effects of Cu-doped ZnO nanoantibiotic against Gram-positive bacterial strains. *PLoS ONE* **16**, e0251082. https://doi.org/10.1371/journal.pone.0251082

Acknowledgements
Authors are thankful to DST, Govt. of India, for providing a FIST grant for SEM facility. Prof. Ramesh Chandra for providing XRD, FESEM, and XPS facilities at Institute Instrumentation Center (IIC), IIT Roorkee, India. Dr. Nazia Tarannum, Department of Chemistry, CCS University Meerut, UP (India) for providing FTIR facility. Dr. Amit K. Chawla, Department of Physics, UPES, Dehradun, India for providing Raman facility, and Central Instrumentation facility, Jamia Milia Islamia, New Delhi, India for Zetasizer analysis in this research work.

Author contributions
All authors contributed to the research concept and study design. The conceptualization and supervision was done by Y.K.G., As.K. and Aj.K. Methodology was done by S.V., J.S., D.P., N.S. Data curation and data analysis was done by Y.K.G., S. V., A.K., D.P. Editing was done by Y.K.G., B.P., As.K. Visualization was done by D.P.,N.S. The original draft preparation was done by S.V. and Aj.K. The final manuscript was read and approved by all authors prior to submission.

Competing interests
The authors declare no competing interests.

Additional information
Correspondence and requests for materials should be addressed to Y.K.G., A.K. or A.K.

Reprints and permissions information is available at www.nature.com/reprints.

Publisher's note Springer Nature remains neutral with regard to jurisdictional claims in published maps and institutional affiliations.